

Correlations in energy in cosmic ray air showers radio-detected by CODALEMA

Ahmed Rebai^a, Pascal Lautridou^a, Alain Lecacheux^b, Olivier Ravel^a

^a*SUBATECH, IN2P3-CNRS/Université de Nantes/Ecole des Mines de Nantes, Nantes, France.*

^b*LESIA, USN de Nançay, Observatoire de Paris-Meudon/INSU-CNRS, Meudon, France.*

Abstract

A study of the response in energy of the radio-detection method of air showers initiated by ultra-high-energy cosmic rays is presented. Data analysis of the CODALEMA experiment shows that a strong correlation can be demonstrated between the primary energy of the cosmic ray and the electric field amplitude estimated at the heart of the radio signal. Its sensitivity to the characteristics of shower suggests that energy resolution of less than 20% can be achieved. It suggests also that, not only the Lorentz force, but also another contribution proportional to all charged particles generated in the development of the shower, could play a significant role in the amplitude of the electric field peak measured by the antennas (as coherence or the charge excess).

PACS: 95.55.Jz; 95.85.Ry; 96.40.-z

Keywords: Radio-detection, Ultra-High-Energy Cosmic Rays

1. Introduction

So far, the study of Ultra-High-Energy Cosmic rays (UHECR) has relied primarily on the use of particle detectors and fluorescence detectors. Today, further improvements are envisaged by supplementing the conventional measures of Extensive Air Showers (EAS). One of them exploits the detection of the transient radio signal induced by the movement of secondary charged particles in the atmosphere. This method is not novel; it emerged in the early 60s, was abandoned in the mid-70s [1] and then re-launched in early 2000. Several experiments (such as Lopes [2], CODALEMA [3], and many new developments[4]), supported by renewed theoretical foundations [5, 6, 7, 8, 9, 10, 11], are now re-investigating the method. Up to now, the techniques of detection and identification of the shower, of reconstruction of arrival directions, of topology of the electric field, and of emission mechanisms have been most often discussed in the literature [12, 13, 14, 15], while the problem of estimating the energy through the radio method was, up to now, only briefly been touched on in the publications [16, 17].

In this work, the emphasis will be on how and with what, a radio-estimator of the energy of the showers can be derived. We show that, subject to adjustments related to the mechanism of radio emission, a robust correlation can be demonstrated between the energy of a cosmic ray derived from the analysis of the distribution of the particles at ground level and the electric fields measured by antennas, and that it provides an energy estimator by the radio method. Section 2 recalls the essential features of the experimental devices, paying attention to the analysis of the particle detectors and to the derivation of the energy of the showers using the CIC method [18]. The radio-detection performances and the essential features of the showers used for the energy comparison are central to Section 3. Section 4 discusses how, from the analysis of the amplitudes of the signals measured by the antenna array, it is possible to extract an observable – the amplitude of the electric field at its center – which depends on the EAS primary energy. The conclusions appear in the last section.

2. Principle of the experiment

2.1. Detector set-up

The CODALEMA experiment is installed at the radio observatory of Nançay, France. Detailed descriptions of the set-up and of the analysis methods of CODALEMA have already been given in earlier publications [19, 20, 21].

The radio set-up consists of an array of 24 short active dipoles distributed on a cross of 600×500 m. It provides an independent measurement of radio-electric field waveforms in an E-W polarization on each antenna (except for 3 that sample in a N-S polarization). The sensor is based on an active dipole using a wide and short radiator [22]. It operates in a frequency bandwidth from 1 MHz to 200 MHz and is sensitive to the galactic noise background [23]. (A second radio-system, the Nançay decameter array, is dedicated to the study of the electric field with a high spatial resolution [24] using 144 tepee antennas, but its results are not discussed in the current study).

The particle detector array is made up of 17 plastic scintillator stations, which are derived from those used by the EAS-TOP experiment of Gran Sasso [25, 26]. These stations are spread over a square grid of 340×340 m with a spacing of 80 m. The station houses 2 photomultipliers (PMT), one working at high gain, the other at low gain, so as to provide an overall dynamics of 0.3 to 3000 Vertical Equivalent Muons (VEM); this unit corresponds to the mean charge deposited by a single muon crossing the scintillator plate vertically. The detection reaches the maximum efficiency for an energy of 10^{16} eV.

The trigger for all the system is provided by the coincident detection of the five central particle detectors leading to an energy detection threshold located around $10^{15.7}$ eV, at the “knee” energy. For each trigger signal, all waveforms of all detectors are digitized (sampling rate of 1 GS/s, duration of 2.56 μ s and recorded. All the sensors are connected to the central acquisition room through coaxial cables.

2.2. Event selection

The off-line analysis is conducted independently for the two detector arrays.

Concerning the radio device, the radio transient is searched for in the antenna waveform through a $24 - 82\text{ MHz}$ frequency bandwidth where the electric field peak value and the arrival time are extracted. If more than 3 radio transients are detected in coincidence, the arrival direction of the electric field (zenith angle θ , azimuth angle ϕ) is reconstructed by considering a planar wavefront. Assuming a decrease in the electric field profile of the form $\varepsilon_0 \exp(-d/d_0)$, four new observables are introduced: the electric field magnitude at the radio shower center ε_0 , the slope parameter of the electric field d_0 , and the impact location of the radio shower center on the ground (x_0, y_0) . During this processing, the standard deviation of the noise on each antenna is used as the measurement error on the electric field. The timing error is estimated to 10 ns, leading to an angular accuracy of reconstructed arrival directions in the range of the degree [27].

The goal of the particle detectors is to provide the arrival direction, the size, the core location of the EAS and an estimation of its energy, which will serve as a reference for the current study. The arrival direction of the particle front (assumed planar) is estimated from the relative arrival time in each particle detector. An analytical NKG lateral distribution [28] is then adjusted on the measured particle densities in the shower frame. If the shower core position falls inside the particle detector array, the event is referred to as internal and the fitted NKG distribution is used to estimate the primary energy using the constant intensity cut (CIC) method [29].

The features of these events, “radio” and “particles”, are then used to identify the coincidences. In this work, the data collected by CODALEMA during 659 days from November 27, 2006 to March 6, 2009 were analyzed. During this period, 143795 triggers were registered. The radio-detected showers were selected according to several successive criteria [27]. Only events “radio” with at least 4 flashed antennas and for which the coincidence, below 100 ns in time and 20° in arrival direction, between the wavefront “particle” and “radio” were retained. These constraints reduced the available statistics to 1386 coincidences. To benefit from an energy estimation as reliable as possible, only “particles” events with footprints located inside the particle detector array, with zenith angles lower than 60° and energies above $10^{16.7}\text{ eV}$, were kept (events referred to as “internal”). At the end of this selection, only 376 coincidences were sufficiently reliable to be used in further analysis. These criteria, translated in energy spectra and in the efficiency curve of radio-detection, are presented in Fig. 1.

2.3. Energy estimation with the particle detectors

The estimation of the shower energy for the particle detectors, relies fundamentally on the information on the deposited charge, and on the time, from the digitized waveform recorded at the trigger occurrence. For this, the main features of the PMT signal (timing t_0 and amplitude V_{max} , are first obtained by fitting it to the following shape:

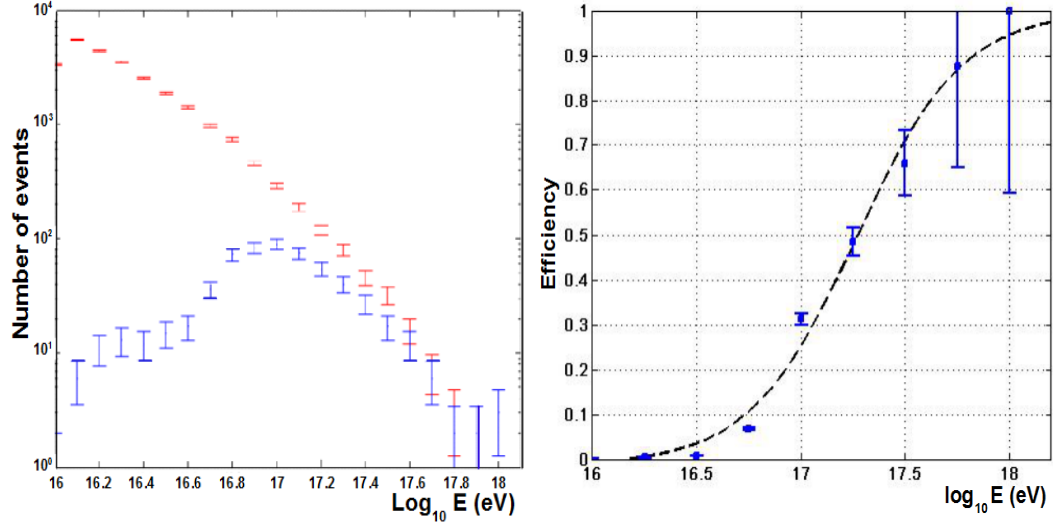


Figure 1: Left: Full energy distribution seen by the particle detector array (red markers) and the subset in coincidence with the radio antenna array (blue markers). Right: “Radio” efficiency (in the east-west polarization state) versus the energy given by the particle detector array.

$$V(t) = V_0 + V_{max} \left(\frac{(t - t_0)e}{n\tau} \right)^n e^{-\frac{t-t_0}{\tau}}$$

where V_0 is the background baseline, which could be taken as constant in the fit interval. The corresponding charge Q is evaluated from the resulting fitted function $V(t)$. For each station, this charge is converted to a VEM number, by calibration from specific counting of the single muons. The VEM number, corresponding to the average value of the measured spectrum corrected by the mean crossing angle 36.9° , serves as calibration factor to convert the charge Q into the equivalent particle density on each detector.

In parallel, the zenith angle θ and azimuth angle ϕ of the shower are obtained by a planar adjustment from the relative time of flight between the different stations. Both angular resolutions (on θ and ϕ) are of the order of 1° for events of energy higher than a few 10^{16} eV, noting that both associated errors are strongly correlated.

Event by event, station positions are projected into the plane perpendicular to the arrival direction and containing the central detector. A MINUIT minimization algorithm, assuming an NKG theoretical shape, performs the reconstruction of the lateral distribution of the particle densities. The core position is projected back into the array plane. Internal events are identified by asking for a larger particle density in internal detectors than in surrounding ones. The total internal surface area of the apparatus is then used for energy and flux estimations.

The estimation of the incident particle energy is performed in two different steps:

The Constant Intensity Cut method (CIC) is used to infer the attenuation length Λ_{att} which expresses the decrease in the shower size $N_e(\theta)$ with increasing zenith angle. For each event with $N_e(\theta)$, an equivalent vertical shower size $N_e(0)$ is extracted from the measured N_e and θ .

Vertical air shower simulations with the AIRES Monte-Carlo code [6], at different energies and for incident protons, provide the correspondence between the primary energy E_{proton} and the mean value of the simulated shower sizes $\langle N_e(0) \rangle$ at each energy E_{proton} .

The usual integral intensities $J(> N_{ec}, \theta)$ (in $m^{-2}.s^{-1}.sr^{-1}$) [30] are calculated for a shower size greater than a given value N_{ec} . The corresponding attenuation curves $N_e(\theta)$ are derived, as well as the corresponding attenuation lengths Λ_{att} . The mean experimental value of Λ_{att} ($188 g/cm^2$) is very close to that extracted from AIRES simulations ($190 g/cm^2$). The incident energy E (eV) is deduced from AIRES simulations, by identifying $N_e(0)$ to the mean value $N_e(0)$ obtained from one hundred shower simulations at a given energy and a given kind of primary ray. Six proton energies in the range $10^{16} - 10^{18}$ eV have been considered, leading to the energy estimation:

$$E_p(eV) = 2.138 \cdot 10^{10} \cdot \langle N_e(0) \rangle^{0.9}$$

The main uncertainty about the energy estimation is due to the shower to shower fluctuations at a fixed energy and is of the order of 30 % at 10^{17} eV. The primary flux, extracted from the data, has been compared to published results in this energy range (Fig. 2). The results are very close to the proton curve, although our setup is probably not sophisticated enough to draw strong conclusions from this result.

3. Analysis of the radio data

3.1. Data processing of the signal radio

As this study relies on the analysis of the amplitude of the transient electric field received by the antenna, during the data processing several corrections are applied to estimate the actual magnitude of the incident electric field. Taking into account these effects, a conversion of the measured voltage amplitude (in V) to an electric field (in V/m) detected by the antenna is achieved.

A numerical filtering of the waveform (24 – 82 MHz band pass filter) is undertaken in order to eliminate the contributions of AM and FM radio transmitters.

A compensation function versus the frequency is introduced to take into account the measured signal attenuation along the length of the cable (up to 380 m) carrying the signal from the antenna to the digitizer and insertion losses due to the connectors.

As the directivity of the radio reception of the dipole located near the ground is not isotropic, a correction of the peak amplitude of the transient signal, based on the arrival direction of the EAS, is applied. This is achieved using the output

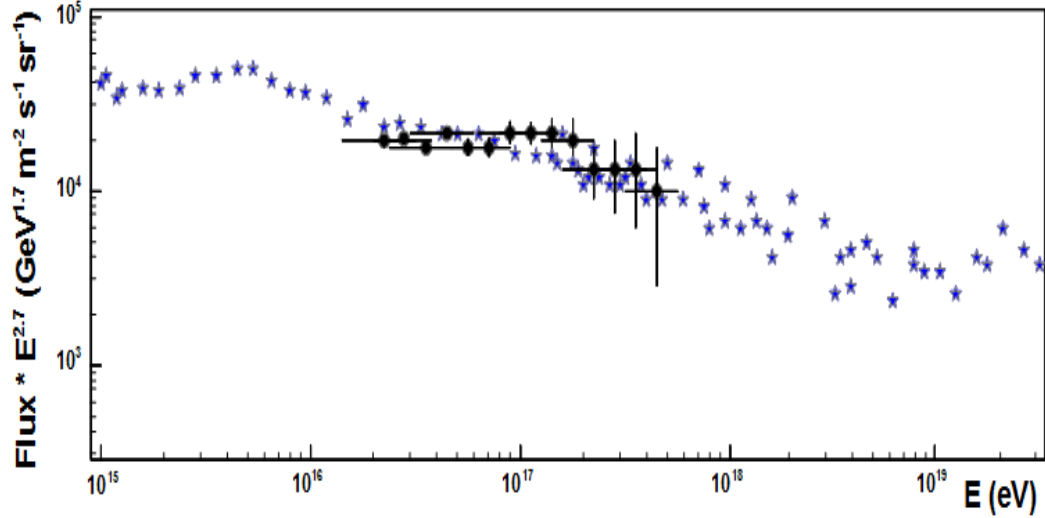


Figure 2: Measured flux $E^{2.7} \times \Phi(E)$ [$\text{GeV}^{1.7} \text{m}^{-2} \text{s}^{-1} \text{sr}^{-1}$] as a function of E (eV). The black circles are our calculations for proton primaries. The blue stars are from cosmic ray data compilations.

results of the EZNEC simulation software [31] for the radiation pattern of the antenna.

In contrast, the effect of the group velocity of the signal during its propagation through the chain of detection, was ignored. Due to the absence of analog filters in our electronic chain, such a correction is not considered critical in the $24 - 82 \text{ MHz}$ band used in this study.

Given the speed of sampling of the waveform digitizer (1 GS/s , analog bandwidth $0 - 300 \text{ MHz}$) and the frequency band used ($24 - 82 \text{ MHz}$), the AD conversion introduces a non-significant deformation of the peak amplitude and no correction was applied.

The signal deformations due to the environment near the sensors (trees, buildings) were also searched for, but analysis did not reveal an important role for this parameter [32].

3.2. Features of selected “radio” events

In practice, the only available knowledge to construct the radio observables is the measured arrival time t_i and the strength ε_i of the radio transients, which are picked up at different locations of the radio-detection area (at antenna positions x_i, y_i). These observables are thus independent of those deduced from the particle detector array.

In agreement with historical observations [1] and recent theoretical developments [5, 6, 7, 8, 9, 10, 11], we used, event by event, an exponential Radio Lateral Distribution Function (RLDF). It describes the radio signal amplitude

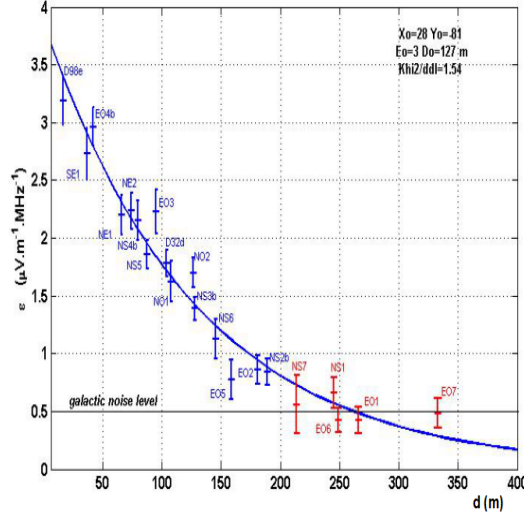


Figure 3: Result of the fit of an RLDF of the form $\varepsilon_0 \exp(-d/d_0)$ for a radio event observed by CODALEMA in the referential of the shower "radio".

as a function of the distance d to the shower axis in the frame of the shower, as an exponential law of the form (Allan's parametrization):

$$\varepsilon_d = \varepsilon_0 \exp\left(-\frac{d}{d_0}\right) \quad (1)$$

With our convention of angles (azimuthal angles $\phi = 0^\circ$ to the north and $\phi = 90^\circ$ to the west, zenith angles θ) and because the detectors are located at the same altitude, this relation can be re-written as:

$$\varepsilon_{d,i} = \varepsilon_0 \exp\left(-\frac{[(x_i - x_0)^2 + (y_i - y_0)^2 - ((x_i - x_0) \cos \theta \sin \phi + (y_i - y_0) \sin \theta \sin \phi)^2]^{1/2}}{d_0}\right) \quad (2)$$

This simplest approach introduces the 4 new ground observables for each shower: (ε_0, d_0) and (x_0, y_0) , respectively the electric field magnitude at the core, the slope parameter of the electric field (the speed at which the transient electrical signal decreases with the distance to the axis), and the impact location of the shower on the ground.

The functional is estimated event by event, providing the coordinates (x_i, y_i) , the signal amplitude ε_i of the tagged antennas, and the zenith and azimuth angles (θ, ϕ) of the radio wavefront reconstructed by a planar fit (which itself uses the arrival time measurements t_i). The fit of the RLDF is computed only for showers having at least 5 tagged antennas, as a consequence of the four free parameters. Figure 3 presents an RLDF reconstructed from a high antenna multiplicity event.

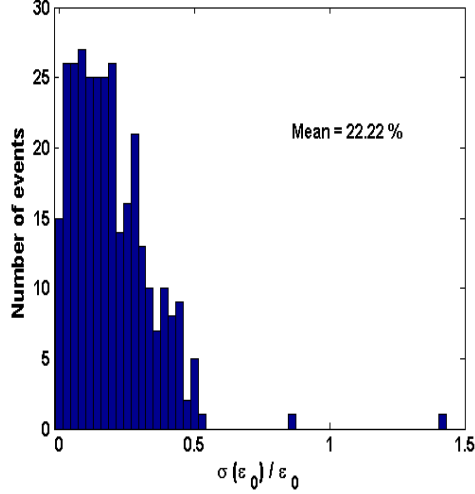


Figure 4: Distribution of the estimated error of the electric field at the shower footprint obtained from Monte Carlo calculations. A average relative error $\sigma(\varepsilon_0)/\varepsilon_0 = 22.22\%$ is obtained, which will be used for the further analysis.

One of the most delicate aspects of the adjustment is to assign an error to the observable ε_0 . This is achieved using the selected “radio” event as an input of a Monte Carlo calculation. For each event, a thousand RLDF fits are repeated, with signal amplitudes ε'_i randomly taken from a Gaussian probability density function centered on the measured values ε_i , within $\pm 3\sigma$ for each tagged antenna. This error is defined as the standard deviation of the measured radio noise on each antenna. During the convergence of the χ^2 process, the observables (ε_0 , d_0) and core position (x_0 , y_0) are left free while the arrival direction (θ , ϕ) and the antenna positions stay fixed. This procedure enables the relevant part of the phase space to be explored and thus the error ε_0 to be estimated on an event by event basis. The results are combined in Fig. 4. By choosing a functional error similar to that used for the particles (not per event), on average a 22 % error affects the estimation of ε_0 [33].

One of the other parameters for the radio-estimator of the energy is the slope parameter d_0 whose distribution is presented in Fig. 5. The peak value of the d_0 distribution is 156 m. About 20 % of the events exhibit a d_0 greater than 400 m. Two potential causes of this tail have been investigated: the malfunction of some antennas and disruptions due to the configuration of the environment near the antennas. After analysis, only 2 % of events were affected by these disturbances [34] and these were removed from the data set.

As will be shown, the other valuable features of “radio” events lie in the distribution of their arrival directions with respect to the geomagnetic axis. It was shown in a previous work [21] that the electric field magnitude depends on the Lorentz force via the vector cross product $\mathbf{v} \wedge \mathbf{B}$, where \mathbf{v} is the vector

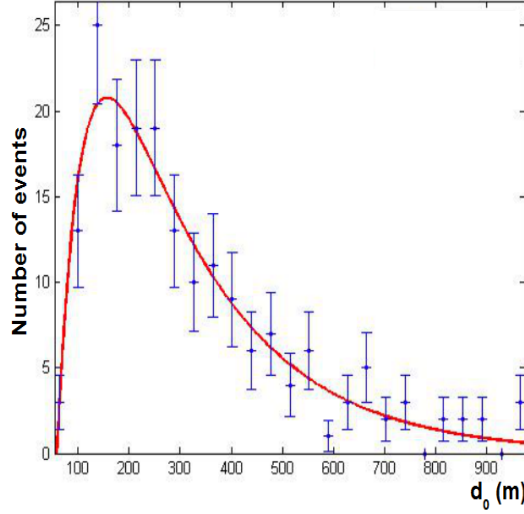


Figure 5: Distribution of the slope parameter d_0 for the events "radio". The red line is to guide the eye.

velocity of the primary particle and \mathbf{B} is the earth's magnetic field (north-south oriented with a zenith angle of 27° at Nançay). With our convention of angles, the projection of the unitary vector of $|(\mathbf{v} \wedge \mathbf{B})_{EW}|$ on the east-west axis can be written as:

$$|(\mathbf{v} \wedge \mathbf{B})_{EW}| = |-\sin \theta \cos \phi \cos 27 - \cos \theta \sin 27| \quad (3)$$

This projection quantifies the influence of this process of emission. The associated distribution of this quantity is depicted in Fig. 6.

4. Electric field and energy correlation

4.1. Radio-estimator of the shower energy

Basically, the electric field radiated should be linked to the energy of the primary particle through the number of secondary charges produced within the shower. According to our data, the only available observables that can be directly related to the shower energy are based on the RLDF parameters (ε_0, d_0) . The simplest assumption suggests using the observables ε_0 , the electric field at the radio shower center, or $\int \varepsilon_0 \exp(-d/d_0) dr = \varepsilon_0 d_0^2$, the integral of the RLDF. Because of difficulties in interpreting huge values of $\varepsilon_0 d_0^2$ for flat RLDFs, this latter observable was rejected. The simplest quantity ε_0 was chosen to study the correlation with the shower energy estimator E_P given by the particle detector array.

Figure 7 shows the scatter plot of ε_0 versus E_P . It exhibits a clear dependence of ε_0 on the primary energy E_P (to improve the clarity of the figure, the

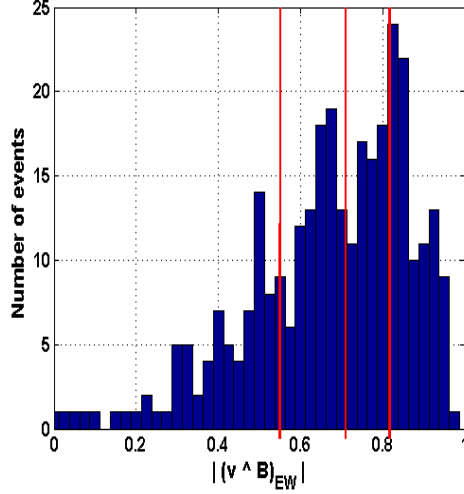


Figure 6: Distribution on the east-west axis of the quantity $|(\mathbf{v} \wedge \mathbf{B})_{EW}|$ for our sample of events. The mean of the distribution is located at 0.67. The windows used in the present study are marked in red. Their corresponding means are 0.40, 0.64, 0.77, and 0.88.

error bars of 30 % for E_P and 22 % for ε_0 are not represented). Indeed, the adjustment of this distribution with the power law $\varepsilon_0 \propto E_P^\gamma$ indicates an almost linear relationship between both quantities (power coefficient $\gamma = 1.03$) in our detection range. Accordingly, we chosen to fit the scatter plot distribution with the simple linear relation:

$$\varepsilon_0 = \alpha E_P + \beta \quad (4)$$

for which the parameters α and β are determined by minimizing, for all events (ε_0, E_P) , the quantity:

$$\chi^2 = \sum_i \frac{[\varepsilon_0 - (\alpha E_P + \beta)]^2}{[\sigma^2(\varepsilon_0) + \alpha^2 \sigma^2(E_P)]} \quad (5)$$

where $\sigma(\varepsilon_0)$ and $\sigma(E_P)$ are the experimental standard deviations of the radio sigma ε_0 and the energy E_P respectively, deduced from CIC analysis and reported on the measurement errors associated with each event.

Inversion of the relationship enables the functional of the calibration in energy E_0 of the radio signal to be extracted in the form:

$$E_0 = \varepsilon_0 / \alpha - \beta / \alpha \quad (6)$$

$$= a \varepsilon_0 + b \quad (7)$$

Discrepancies between both observables E_0 and E_P have been investigated through the distribution of their relative differences, defined as:

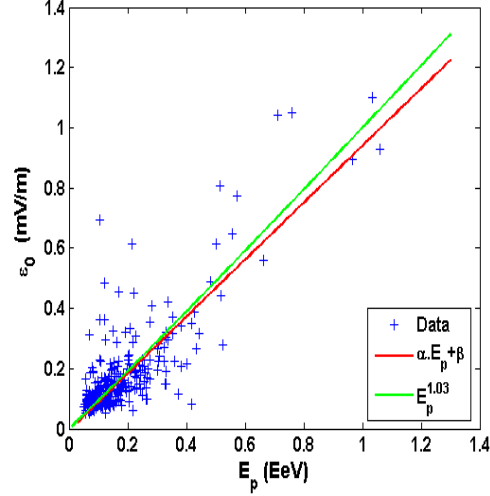


Figure 7: Raw scatter plot of the electric field ε_0 at the shower core versus the primary energy E_P (for the readability of the figure the error bars of 30 % for E_P and 22 % for ε_0 are not represented). The adjustment of the data with the power law $E_P^{1.03}$ is shown as a green line while the linear adjustment is shown in red.

$$(E_P - E_0)/E_P \quad (8)$$

and its Standard Deviation (SD) given by (with μ , the mean of the distribution):

$$\sigma((E_P - E_0)/E_P) = \sqrt{\frac{1}{N-1} \sum ([(E_{Pi} - E_{0i})/E_{Pi}] - \mu)^2} \quad (9)$$

The typical form of distributions $(E_P - E_0)/E_P$ is presented in Fig. 8. The analysis of the width by a Gaussian fit was not considered relevant because, as shown below, it is precisely the deviations from the main peak of the events (the events in the tails) that reveal the interesting effects.

4.2. Correction factors

In a previous article, we highlighted a significant asymmetry [21] of the EAS detection (in the east-west polarization) between the south and north sectors of the sky. It was shown that the electric field magnitude depends on the Lorentz force via the vector cross product $\mathbf{v} \wedge \mathbf{B}$. To take this result into account, the estimator ε_0 has been corrected by the inverse of the projection of the Lorentz force along the east-west polarization (Fig. 9). In other words, we assume that the observed electric field ε_0 is proportional to the actual shower energy E and that two detected showers of the same primary energy (and of the same nature) will produce two different radio signals depending on their angle with the geomagnetic axis, by following dependencies of the form:

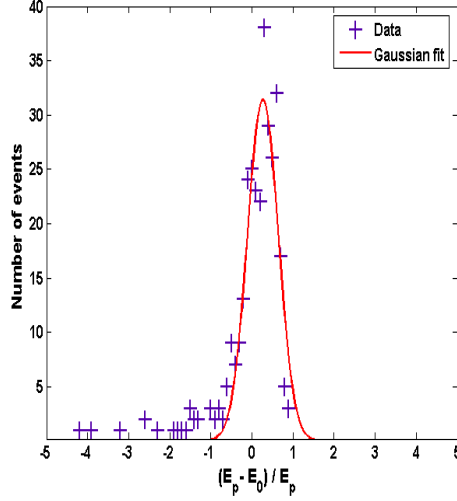


Figure 8: Distribution of the fractional difference between the energy estimated with the scintillator array and the energy estimated with the antenna array, obtained after calibration and for the full sample of events (blue crosses). The standard deviation is 31 % with $c = 0.95$ (see below). The red line shows a Gaussian fit made in the interval $[-1, 1]$.

$$\varepsilon_0 \sim E |(\mathbf{v} \wedge \mathbf{B})_{EW}| \quad (10)$$

$$\varepsilon'_0 \sim E |(\mathbf{v}' \wedge \mathbf{B})_{EW}| \quad (11)$$

The examination of the corresponding scatter plot (E_P, E_0) , presented in Fig. 9, highlights a new phenomenon. With this correction, the new locations of the events located close to the earth's magnetic field direction ($|(\mathbf{v} \wedge \mathbf{B})_{EW}| < 0.1$) deviate significantly from the raw distribution of Fig. 7, exhibiting unrealistic energy with the radio. In addition, with the assumption of a purely geomagnetic emission process, these events should not be radio-detected, particularly noting that their estimated CIC energy shows nothing unusual. This suggests that the corrected amplitudes are obviously overestimated, and that a further correction must be introduced, to produce observable signals, especially when the Lorentz contribution becomes weak. Moreover, in the case of a higher counting statistics (larger counting time and detector surface), far above the detection threshold, the rate of detected events around the direction of the geomagnetic field should join to those of the other arrival directions. The lack of a correction term additional would lead to overestimate the energy and to strongly modify the energy spectrum. To account from these remarks, we introduce a constant term c in our previous prescription, making the assumption that the observed electric field ε_0 can also be proportional to the actual shower energy E by:

$$\varepsilon_0 \sim E c \quad (12)$$

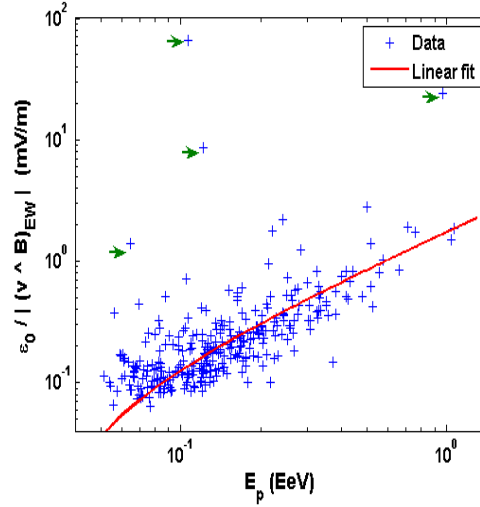


Figure 9: Scatter plot of the corrected electric field $\varepsilon_0 / |(\mathbf{v} \wedge \mathbf{B})_{EW}|$ versus the primary energy E_P . The linear adjustment is shown in red. The green arrows show some of the typical over-corrected events. The systematic analysis of their features indicates that all these events have arrival directions near the earth's magnetic field direction ($|(\mathbf{v} \wedge \mathbf{B})_{EW}| < 0.1$). (These points are removed for the linear fit of the scatter plot).

the superposition of both contributions causing the dependence:

$$\varepsilon_0 \sim E |(\mathbf{v} \wedge \mathbf{B})_{EW}| + E c \quad (13)$$

leading to modify ε_0 toward:

$$\varepsilon_0 \rightarrow \varepsilon_0 / (|(\mathbf{v} \wedge \mathbf{B})_{EW}| + c) \quad (14)$$

At first glance, the physical meaning of this additional contribution is tricky, but it should be noted that, with the quantity $|(\mathbf{v} \wedge \mathbf{B})_{EW}|$ ranging from 0 to 1, $c = 0$ corresponds to a purely geomagnetic contribution, while a high c value (e.g. $c > 6$) should represent the case for which the geomagnetic emission becomes negligible compared to the second effect. Thus, a high c value must induce a behavior similar to that observed without correction.

The result is depicted in Figure 10, which presents the standard deviation of the $(E_P - E_0)/E_P$ distribution as a function of c and for several bins in $|(\mathbf{v} \wedge \mathbf{B})_{EW}|$.

With the full sample of events (blue markers on figure 10), the result seems monotonous with a weak minimum obtained around $c = 0.95$. Concerning the sub-samples, except for the two windows of lowest values in $|(\mathbf{v} \wedge \mathbf{B})_{EW}|$, the raw values of the standard deviations (indicated by stars at the right side of the figure 10) are bigger than when the corrections are applied. The widths of the distributions depend clearly from the direction of arrival of the showers with respect to the magnetic field direction $|(\mathbf{v} \wedge \mathbf{B})_{EW}|$ and with c .

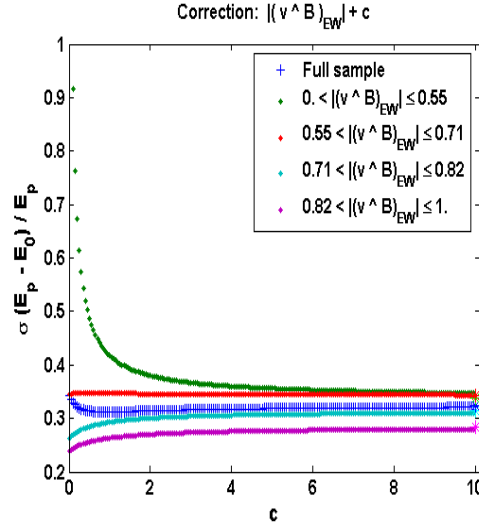


Figure 10: Evolution of the Standard Deviation of the distribution $(E_P - E_0)/E_P$ with the correction factor $1/(|(\mathbf{v} \wedge \mathbf{B})_{EW}| + c)$ as a function of c and for several windows of $|(\mathbf{v} \wedge \mathbf{B})_{EW}|$. The blue line represents the whole sample of events. The start located $c = 10$ show the SD obtained without applying a correction.

For the wide angles with the geomagnetic direction, the smallest dispersions are achieved when $c = 0$. This suggests that the geomagnetic correction is significant and thus that this emission process is clearly dominant in this region. On the contrary, for the events arriving near the geomagnetic axis, large values of c are called for. With regard to these events, the low values of c induce deviations that reflect the larger gaps compared to the main peak of the distribution. (This particular behavior explains why a Gaussian fit of the distributions $(E_P - E_0)/E_P$ was not used for the analysis.) For these events, the contribution in c , directly correlated to the energy of the shower, becomes significant, compared to the geomagnetic effect. The remarkable values reached for the standard deviations are summarized in Table 1 with their corresponding values of c .

These results demonstrate that there is a strong correlation between the radio signal, deduced using the peak amplitude of the extrapolated electric field at the shower core, and the energy of the shower obtained via the CIC method (although the latter is estimated without great accuracy). The observed variations in function of $|(\mathbf{v} \wedge \mathbf{B})_{EW}| + c$ confirm the robustness of the correlation of the radio signal with the actual energy of the shower and suggest strongly that the radio signal is made of the mixture of several emission effects.

The association of the parameter c to an existing electric field was then investigated. Because of considerations of symmetry of the electric field according to the axis of the radio signal, we have focused on the contribution of an electric field component whose orientation would follow the radio shower axis (eg. the one induced by the net charge of the shower and which would remain

$\sigma((E_P - E_0)/E_P)$	Correction $ (\mathbf{v} \wedge \mathbf{B})_{EW} $ alone	Correction $ (\mathbf{v} \wedge \mathbf{B})_{EW} + 0.95$	No correction
Full sample (293 events)	0.34	0.31 (minimum)	0.32
$< (\mathbf{v} \wedge \mathbf{B})_{EW} \geq 0.4$ (70 events)	2.27	0.42	0.34
$< (\mathbf{v} \wedge \mathbf{B})_{EW} \geq 0.64$ (79 events)	0.34	0.35	0.34
$< (\mathbf{v} \wedge \mathbf{B})_{EW} \geq 0.77$ (68 events)	0.26	0.29	0.31
$< (\mathbf{v} \wedge \mathbf{B})_{EW} \geq 0.88$ (77 events)	0.23	0.26	0.28

Table 1: Standard deviation of $(E_P - E_0)/E_P$ as a function of the correction factor c varying arbitrarily from 0 to 10. In Gaussian approximation, the error on the standard deviation can be given by $\sqrt{2} \sigma^2 / \sqrt{N-1}$ ($N \approx 70$ for the subsets).

basically proportional to the energy of the shower). To address this possibility, we changed the term c by:

$$\varepsilon_0 \sim E |(\mathbf{v} \wedge \mathbf{B})_{EW}| + E c |\sin \theta \sin \phi| \quad (15)$$

The effect of this correction is depicted in Figure 11, which presents the standard deviation of the $(E_P - E_0)/E_P$ distribution as a function of c and for the same windows as in $|(\mathbf{v} \wedge \mathbf{B})_{EW}|$. It clearly reflects a lower quality of the correlation and suggests that the simple correction $|(\mathbf{v} \wedge \mathbf{B})_{EW}| + c$ captures better the experimental observations.

A scalar emission mechanism was then searched for, particularly noting that our observations were compatible with some recent theoretical and experimental interpretations [14, 35, 36]. For example, the charge excess mechanism induces features that are in qualitative agreement with our present observations: the induced emission depends on the charges produced in the shower (and so from the energy); its weight in the total emission process should increase when the geomagnetic contribution, governed by $\mathbf{v} \wedge \mathbf{B}$, decreases.

On another hand, by noting that $|(\mathbf{v} \wedge \mathbf{B})_{EW}| + c$, can be rewritten $|(\mathbf{v} \wedge \mathbf{B})_{EW}| (1 + c/|(\mathbf{v} \wedge \mathbf{B})_{EW}|)$, one could understand also the second term as an amplification effect, inversely proportional to the Lorentz force. Taking into account the forces acting on the secondary particles in the pancake, it could suggest a coherence effect modulated by the Lorentz force. This process, being similar to that caused by the deflection of a magnetic dipole on particles in an accelerator beam line, could increase when the secondary particles are less dispersed by the Lorentz force (i.e. at small $|(\mathbf{v} \wedge \mathbf{B})_{EW}|$) during their propagation.

4.3. Calibration relationship

Table 2 summarizes the calibration factors (a, b) for our set-up, with and without correction. Taking advantage of the full event feature to deduce ε_0 , the

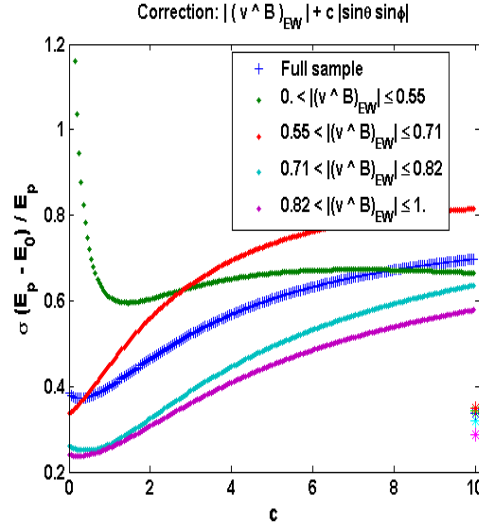


Figure 11: Evolution of the Standard Deviation of the distribution $(E_0 - E_P)/E_P$ with the correction factor $1./(|(\mathbf{v} \wedge \mathbf{B})_{EW}| + c |\sin \theta \sin \phi|)$ as a function of c and for several values of $|(\mathbf{v} \wedge \mathbf{B})_{EW}|$. The blue line represents the whole sample of events. The start located at $c = 10$ show the SD obtained without applying a correction.

Full sample (293 events)	a (EeV/mV)	b (EeV)
No correction	1.03 ± 0.05	0.0083 ± 0.0004
Correction $ (\mathbf{v} \wedge \mathbf{B})_{EW} $ alone (with $c = 0$)	0.59 ± 0.06	0.0230 ± 0.0005
Correction $ (\mathbf{v} \wedge \mathbf{B})_{EW} + 0.95$ (minimum)	1.59 ± 0.09	0.0152 ± 0.003

Table 2: Energy calibration coefficients in function of the the correction factor in the cases "without correction", "with the geomagnetic effect alone", "with a scalar contribution (c=0.95) added to the geomagnetic effect".

calibration can be expressed by:

$$E_0 = \frac{a}{(|(\mathbf{v} \wedge \mathbf{B})_{EW}| + c)} \varepsilon_0 + b \quad (16)$$

According to the different corrections, the slope parameter a of the line varies by about 37 %. Similarly, for the value of the y-intercept, a relative variation of b up to 36 % is observed. The latter could be more related to the noise seen by the antennas which acts as an offset in the amplitude of the radio-signal. As this noise contribution is not constant, it can be only partial. Both parameters depend mainly on the absolute calibration of the electric field antennas. At present, it is not determined, in absolute terms, to better than a factor of 2. Nevertheless, the relative reference remains identical for each antenna of the entire installation. Furthermore, the calibration depends on the frequency bandwidth that is being analyzed, and on the frequency response of the detection chain. This is, in principle, corrected but the line parameters also depend on

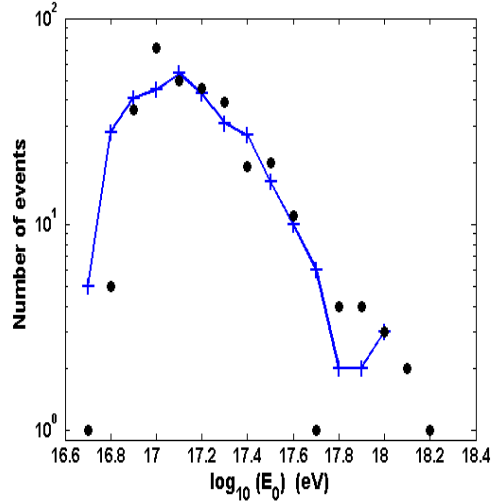


Figure 12: Comparison of energy spectra for events “radio”. In blue, the spectrum obtained by assigning to the events “radio” the energy given by the particle detectors (cf. Fig 1, left panel); in black, the spectrum obtained after calibration of the radio signal using the correction $(|(\mathbf{v} \wedge \mathbf{B})_{EW}| + 0.95)$.

the frequency content of the transient. Thus, it is likely that it will be necessary to readjust the terms of the calibration relationship for each detector system. This suggests that the implementation of calibration methods, accurate enough and independent of the specific characteristics of the detectors, will only be possible when a full model of the radio emission process becomes available. The two energy spectra deduced from the CIC analysis and calibration of radio, are presented in Figure 12. They indicate a very satisfactory consistency between both observables of the energy of the primary.

4.4. Energy resolution

One of the most challenging aspects of the calibration procedure is to assign an error to the observable E_0 provided by the previous outputs. This has been addressed by studying the effect of $\sigma(E_0)/E_0$ in a simulated distribution $(E_P - E_0)/E_P$ ($\sigma(E_P)/E_P$ being fixed), while noting that this procedure does not allow the error on E_0 to be explored, on an event by event basis. A random distribution in energy E of the events is adjusted to the experimental data (cf. left panel of Fig. 1). The pairs (E_P, E_0) are then derived. For each energy coming E , the associated energy E_P assigned to the particle detector is taken randomly from a Gaussian probability density function centered on E with $\pm 3\sigma$ and with $\sigma(E_P)/E_P$ fixed; similarly for the associated energy E_0 of the radio-estimator with $\pm 3\sigma$ and with the $\sigma(E_0)/E_0$ chosen for the study. The distribution $(E_P - E_0)/E_P$ is built step by step and finally its standard deviation is calculated. No correction with the geomagnetic effect is introduced because

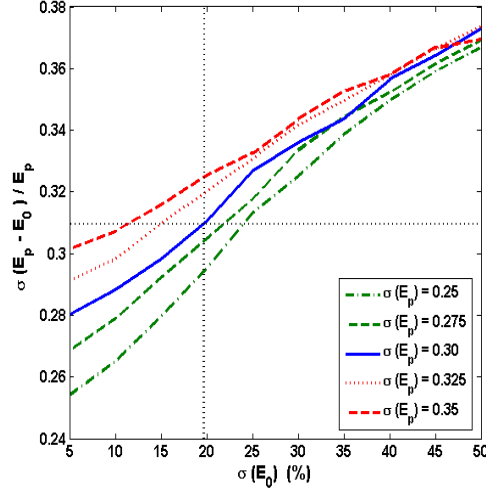


Figure 13: Reconstructed RMS of the simulated distributions $(E_0 - E_P)/E_P$ as a function of $\sigma(E_0)/E_0$ and for 5 values of $\sigma(E_P)/E_P$ (0.25, 0.275, 0.3, 0.325, 0.35). The solid blue line in blue corresponds to the current energy resolution of 30 % of the particle detector array.

the Monte Carlo provides E_0 directly. The results of the SD are combined in Fig. 13 versus $\sigma(E_0)/E_0$. With $\sigma(E_P)/E_P = 30\%$, a relative error below 20 % is obtained for E_0 .

One of the recurring issues with this kind of calibration is whether the experimental result is the consequence of a strong hidden correlation between the two energy observables, like that which might arise from the uncertainty about the depth of the first interaction. Here, one fundamental aspect could differentiate the radio from the particles measurements. While the particle density is sampled at a fixed depth of the shower, the radio signal integrates its development in the atmosphere. In the energy range specifically studied here, the whole development (including at the X_{max} depth) is always seen by the antennas. One can suppose, therefore, that this phenomenon will not produce this bias in our “radio” observation.

5. Conclusion

We presented an attempt to estimate the energy of primary cosmic rays using the measurement of the radio-electric field associated with the air showers. We took advantage of the electric field ε_0 deduced at the core position of the shower through an exponential Radio Lateral Distribution Function of the electric field. We showed that a linear relationship can be found between this observable and the inferred energy of the particle detectors, allowing the calibration of the radio-detection method in the MHz range.

Taking into account previous results on the geomagnetic effect, we then emphasized the utility to correct the electric field amplitude by this effect. The study of the distributions of relative energies, built from the radio and particles method, led us to search for adequate relationships for the correction. The observed variations proved that the correlation was robust and sensitive enough to be improved by adjusting some parameters. This led us to consider the idea of a mix of several emission effects. In the present state of the statistic, a second correction proportional to the energy of shower (scalar contribution) seems justified, as for instance coming from a coherence effect, although our preliminary interpretations remain compatible with the recent inclusion of new effects in the emission processes, like the charge excess.

Combined with other detection performances (cost, ease of use, duty cycle, etc.) our first estimate of the energy resolution (rather below 20 %) suggests that the method could be particularly attractive. With the limited data set available, the absolute calibration of the energy remains difficult even though it is largely compatible with the measurement of the energy supplied by the particle detectors, and therefore usable. In addition, it is not clear that we should work in the referential of the particles or that provided by radio signals. However, the principle of the correction doesn't depend of the form of the Radio Lateral Distribution Function of the electric field. We expect that the use of a more relevant RLDF still increases the correlation, and thus that our present energy resolution correspond to a pessimistic estimate for the radio-detection method.

More data should improve obviously the proposed approach, but there is already an indication of a very interesting energy resolution and a hope that the radio signal could directly depend of the simple parameters considered. This could also be a significant advantage of the radio method.

References

References

- [1] H.R. Allan, in: Progress in elementary particle and cosmic ray physics, ed. by J.G. Wilson and S.A. Wouthuysen (North Holland, 1971) 169.
- [2] A. Badea et al, Proceedings of CRIS2004, Nucl. Phys. Proc. Suppl. 136 (2004) 384.
- [3] O. Ravel et al, Nucl. Instrum. Meth. A 518 (2003) 313.
- [4] UHECR2012 Symposium, CERN, Feb. 2012, Book of abstracts , <http://2012.uhecr.org>.
- [5] H. Falcke , P. W. Gorham , Astropart. Physics 19 (2003) 477-494.
- [6] M. Du Vernois, B. Cai, et D. Kleckner, Proc. of the 29th ICRC, Pune (India), vol. 8. 2005.

- [7] P. W. Gorham et al., arXiv:0705.2589v1 [astro-ph] 17 may 2007.
- [8] O. Scholten, K. Werner, and F. Ruydi, *Astropart. Phys.* 29, 94 (2008).
- [9] N. Meyer-Vernet et al., *Astronomy & Astrophysics*, 480,15-25 (2008).
- [10] J. Chauvin et al., *Astroparticle Physics* 33 (2010) 341–350.
- [11] V. Marin et al., *Asptropart. Phys.*, ISSN 0927-6505, 10.1016/j.astropartphys.2012.03.007.
- [12] D. Ardouin et al, *Astropart. Phys.* 31 (2009) 19–200.
- [13] W.D. Apel, et al. - LOPES collaboration, 2010, *Astroparticle Physics* 32, 294-303.
- [14] V. Marin for the CODALEMA collaboration, *Proc. of the 32nd ICRC*, Beijing, 2011.
- [15] B. Revenu for the PIERRE AUGER collaboration, *Proc. of the 32nd ICRC*, Beijing, 2011.
- [16] A. Horneffer, et al., *Proc. of the 30th ICRC*, Mérida 2007.
- [17] P. Lautridou for the CODALEMA collaboration, *Nuclear Instruments and Methods in Physics Research A* 604 (2009) S1–S19.
- [18] B. G. Kristiansen, et al. *Cosmic Rays of Super high Energies*. Atomizdat, 1975. (Russia).
- [19] D. Ardouin, et al., *Nuclear Instruments and Methods In Physics Research Section A* 555 (2005) 148.
- [20] D. Ardouin et al., *Astroparticle Physics* 26 (2006) 34–350.
- [21] D. Ardouin, et al., *Astroparticle Physics* 31 (2009) 192.
- [22] D. Charrier and the CODALEMA collaboration, in: *IEEE Antennas and propagation Society International Symposium*, Honolulu, Hawai June 10–15, 2007.
- [23] J.Lamblin for the CODALEMA collaboration, *Proc. of the 30th ICRC*, Mérida 2007.
- [24] A. Lecacheux, A.Bellétoile for the CODALEMA collaboration, *Proc. of the 31st ICRC*, Lodz 2009.
- [25] M. Aglietta, et al., *Nuclear Instruments and Methods in Physics Research, Section A* (1993) 1, 31–321.
- [26] G. Agnetta, et al., *Nuclear Instruments and Methods In Physics Research Section A* 570 (2007) 1, 22 – 35.

- [27] O. Ravel for the CODALEMA collaboration, Nuclear Instruments and Methods In Physics Research Section A 662 (2012) S89-S94.
- [28] T. G. Gaisser, Cosmic Rays and Particle Physics, Cambridge University Press 1990.
- [29] A. A. Chilingarian, et al., Proc of the 27th ICRC, Hamburg, Germany 2001.
- [30] J. Alvarez-Muniz, R. Engel, T. Gaisser, J. Ortiz, et T. Stanev, Physical Review D 66 (2002) no. 12, 123004.
- [31] D. Charrier, et al., Nuclear Instruments and Methods In Physics Research Section A 572 (2007) 481.
- [32] T. Garçon for the CODALEMA collaboration, Nuclear Instruments and Methods In Physics Research Section A 662 (2012) S69-S71.
- [33] A. Rebai for the CODALEMA collaboration, Some recent results of the Codalema Experiment, Proc. of the annual meeting of the French Society of Astronomy & Astrophysics SF2A, Paris, June 2011, G. Alecian, K. Belkacem, R. Samadi and D. Valls-Gabaud (eds).
- [34] T. Garçon for the CODALEMA collaboration, in M. Heydari-Malayeri, C. Reylé, R. Samadi(Eds.), Proc. of the SF2A2009.
- [35] K.D. de Vries, A.M. van den Berg, O. Scholten, K. Werner, Phys. Rev. Lett.107:061101, 2011.
- [36] K. Werner, K. D. De Vries, and O. Scholten, arXiv:1201.4471v1[astro-ph.HE], 21 Jan 2012.